

Evaluation of several first-principles closure models for Hall thruster anomalous transport

Thomas A. Marks* and Benjamin A. Jorns.†
 University of Michigan, Ann Arbor, MI, 48109

Five first-principles models of the Hall thruster anomalous electron transport are evaluated. These models are derived assuming that this transport derives from an ion-acoustic-like instability and that the energy at which this instability saturates scales with the drift kinetic energy. It is assumed that the wave loses energy primarily due to convection as the ions move downstream. The effect of secondary damping mechanisms, including classical collisions and Landau damping, are investigated. The models are incorporated into an axisymmetric fluid model of a Hall thruster and a 9 kW-class magnetically shielded Hall thruster is simulated. It is found that the best agreement with experiment is obtained when the secondary damping mechanisms are insignificant compared to convection. The predicted efficiencies agree with experimental values to within 10%, but the simulated ion velocity profiles are more relaxed than the measured values. These both stem from the fact that the anomalous collision frequency predicted by these models attains a minimum near the ion stagnation point, yielding electric fields which peak further upstream than the experimentally-observed values. The results of these simulations are discussed in the context of further anomalous transport closure modeling efforts.

I. Nomenclature

q	=	Fundamental charge (1.6×10^{-19} C)
m_e	=	Electron mass (9.1×10^{-31} kg)
ϵ_0	=	Permittivity of free space (8.854×10^{-12} F/m)
\hat{z}	=	Axial coordinate
\hat{r}	=	Radial coordinate
$\hat{\theta}$	=	Azimuthal coordinate
$\hat{\parallel}$	=	Field-parallel coordinate
$\hat{\perp}$	=	Field-perpendicular coordinate
ν_{AN}	=	Anomalous collision frequency (s^{-1})
ν_{sj}	=	Momentum transfer collision frequency of species s by species j
n_s	=	Density of species s
\mathbf{u}_s	=	Velocity vector of species s (m/s)
\mathbf{j}_s	=	Current density of species s (A/m ²)
T_s	=	Temperature of species s (J)
\mathbf{E}	=	Electric field vector (V/m)
\mathbf{B}	=	Magnetic field vector (T)
ω_{ce}	=	Electron cyclotron frequency (rad/s)
ω_{pe}	=	Plasma frequency (rad/s)
Z	=	Density-averaged ion charge number
v_{de}	=	Electron $E \times B$ drift speed (m/s)
c_s	=	Ion sound speed (m/s)
c_e	=	Electron sound speed (m/s)
M_e	=	Electron Mach number
W	=	Wave energy density (J/m ³)

*PhD. Candidate, Department of Aerospace Engineering, Student Member AIAA

†Associate Professor, Department of Aerospace Engineering, Associate Fellow AIAA

γ = Instability growth rate (s^{-1})

II. Introduction

PREDICTIVE models of Hall effect thrusters are a longstanding goal of the spacecraft electric propulsion (EP) community. These spacecraft propulsion devices have long been employed for satellite station-keeping but have increasingly been baselined for deep space applications, both crewed[1–3] and uncrewed[4, 5]. These missions require higher power levels and longer lifetimes than have been typical for Hall thrusters in the past, and these requirements push the limits of what ground testing in a vacuum chamber can achieve. Hall thrusters are known to perform differently when tested in a vacuum chamber than when flown in space, and these facility effects become more prominent at higher powers[6, 7]. This complicates our efforts to extrapolate observed behavior on the ground to in-space performance. Additionally, verifying the expected lifetime of these thrusters means running them in a vacuum chamber for thousands of hours in order to demonstrate that the rate at which the thruster surfaces erode is within expected limits.

Modelling and simulation have the potential to alleviate this issues. Predictive Hall thruster models would speed up the early design of new thrusters by allowing a number of design iterations to be tested before any ground testing is needed. Additionally, once a model has been validated against ground test performance, it can be used to predict the on-orbit behavior of the thruster. They can even help accelerate thruster wear testing by predicting erosion rates, reducing the need for the lengthy and expensive lifetime tests. However, Hall thruster models are not currently predictive. This means that, given a device geometry and an operating condition, i.e. discharge voltage, mass flow rate and magnetic field configuration, we are currently unable to predict how that thruster will perform with any certainty. This stems from a lack of understanding of some of the underlying Hall thruster physics. Most notably, electrons in Hall thruster are known to transit across the applied magnetic field lines at least an order of magnitude faster than what classical plasma physical theory predicts. The rate and amount of this cross-field electron transport has a direct impact on the strength of the electric field which accelerates the plasma and produces thrust. The electric field in turn governs the amount of plasma heating, and thus controls the amount of ionization that occurs within the thruster. As a result, without the ability to account self-consistently for this so-called “anomalous” electron transport, it is impossible to predict thruster performance and plasma properties from geometry and operating conditions alone.

Many researchers[8–14] have developed models for this phenomenon. However, none have yet proven predictive. In this work, we attempt to do the same, deriving several novel first-principles models of the anomalous electron transport. We calibrate these models to match the discharge current of a 9-kW class Hall thruster and then evaluate how well they are able to match experimental measurements of thrust, anode efficiency, and ion velocity profiles.

To this end, this paper is organized as follows. In Sec. III, we review the problem of anomalous transport in a fluid framework. In Sec. IV, we introduce the physical model underlying our suite of models and introduce the five models we employ in this work. Next, in Sec. V, we describe our methods, including the thruster being simulated and the code used to simulate it, and the model calibration procedure. In Sec. VI, we present our results and in Sec. ??, we discuss these results in the context of model extensibility.

III. The problem of anomalous transport in Hall thrusters

To begin, we review the need to anomalous transport simulations of Hall thrusters that employ a fluid approximation for electrons. In Fig. 1 we show the basic principle of operation of a Hall thruster. A voltage is applied from a conducting anode to a hollow cathode. Electrons emitted by the cathode stream toward the anode, but are arrested in their motion by an applied radial magnetic field. This sets up a strong axial electric field, which when crossed with the magnetic field induces the electrons to rapidly orbit the thruster channel in the so-called *Hall drift*. These orbiting electrons collide with neutral atoms injected at the anode, ionizing them. The resulting ions are accelerated out of the device, producing thrust. Collisions with neutrals and ions allow some electrons to make it to the anode, but the amount of electron current observed to reach the anode is much higher than these collisions alone can account for. This enhanced transport is what we seek to find a model for. While this effect is likely kinetic in origin, we can account for it in a fluid model via an effective “anomalous” collision frequency. To see how this arises, we first consider the fluid electron momentum equation.

$$\frac{\partial}{\partial t}(m_e n_e \mathbf{u}_e) + \nabla \cdot (m_e n_e \mathbf{u}_e \otimes \mathbf{u}_e) = -q n_e (\mathbf{E} + \mathbf{u}_e \times \mathbf{B}) - \nabla \cdot \mathbf{\Pi}_e - \nu_{e,c} m_e n_e \mathbf{u}_e \quad (1)$$

In the above, m_e is the electron mass, n_e is the electron number density, \mathbf{u}_e is the electron velocity, q is the fundamental charge, \mathbf{E} is the electric field, \mathbf{B} is the magnetic field, $\mathbf{\Pi}$ is the electron pressure tensor, and $\nu_{e,c}$ is the classical electron

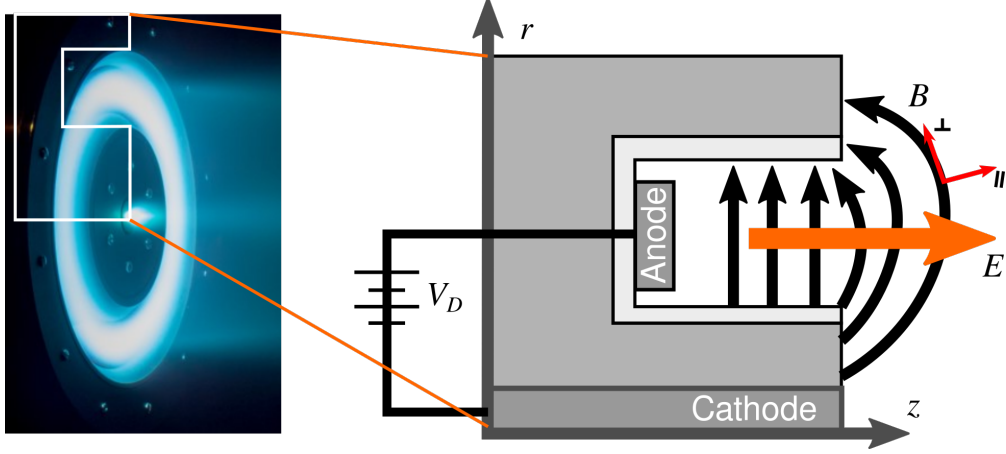


Fig. 1 Diagram of a Hall thruster, showing both Cartesian and field-aligned coordinate systems

collision frequency. If we neglect the electron inertial terms (the left-hand side of Eq. 9), as is commonly done in Hall thruster models, we arrive at the generalized Ohm's law

$$\mathbf{j}_e = \frac{q^2 n_e}{m_e \nu_{e,c}} \left[\mathbf{E} + \mathbf{u}_e \times \mathbf{B} + \frac{\nabla \cdot \mathbf{\Pi}_e}{q e n_e} \right] \quad (2)$$

Here, $\mathbf{j}_e = -q n_e \mathbf{u}_e$ is the electron current density vector. We now further assume that the electron pressure term is isotropic, such that $\nabla \cdot \mathbf{\Pi}_e = \nabla(n_e T_e)$, and that the plasma is axisymmetric, so that for any quantity Q , $\nabla_\theta Q = 0$. We then decompose Eq. 2 into field-parallel (\parallel), field-perpendicular (\perp), and azimuthal components ($\hat{\theta}$):

$$\mathbf{j}_e = j_{e,\parallel} \hat{\parallel} + j_{e,\perp} \hat{\perp} + j_{e,\theta} \hat{\theta} \quad (3)$$

$$j_{e,\parallel} = \frac{q^2 n_e}{m_e \nu_{e,c}} \left[E_{\parallel} + \frac{\nabla_{\parallel} n_e T_e}{q n_e} \right] \quad (4)$$

$$j_{e,\perp} = \frac{\nu_{e,c}}{\nu_{e,c}^2 + \omega_{ce}^2} \frac{q^2 n_e}{m_e} \left[E_{\perp} + \frac{\nabla_{\perp} n_e T_e}{q n_e} \right] \quad (5)$$

$$j_{e,\theta} = \Omega_e j_{e,\perp} \quad (6)$$

In the above, $\omega_{ce} = q|\mathbf{B}|/m_e$ is the electron cyclotron frequency. Furthermore, if the electrons are magnetized, $\nu_{e,c}^2 \ll \omega_{ce}^2$, so the perpendicular component of the Ohm's law reduces to

$$j_{e,\perp} = \frac{\nu_{e,c}}{\omega_{ce}^2} \frac{q^2 n_e}{m_e} \left[E_{\perp} + \frac{\nabla_{\perp} n_e T_e}{q n_e} \right] \quad (7)$$

Thus, we can see that a higher electron collision frequency $\nu_{e,c}$ leads directly to a higher cross-field electron current density $j_{e,\perp}$. So, if we want to increase the amount of cross-field current in order to improve the agreement between simulations and experiment, we can introduce an additional anomalous collision frequency term ν_{AN} such that $\nu_e = \nu_{AN} + \nu_{e,c}$. To estimate this parameter, we require a "closure model", i.e. a model which relates ν_{AN} to other fluid plasma parameters, such as the electric field, electron temperature, ion velocity, and plasma density. We now turn to explaining how we derived several closure models for the anomalous collision frequency.

IV. Anomalous transport modeling framework

In this work, we investigate several closure models derived from a common framework. We assume that the anomalous electron transport seen in Hall thrusters emerges as a consequence of microturbulence. The instability derives its energy from the Hall drift and thus acts as an effective drag force on the electrons in the azimuthal direction.

This in turn induces cross-field drift toward the anode. To begin, we return to the electron fluid momentum equation (Eq. 9), this time separating the electric field into number density into mean and fluctuating components

$$\mathbf{E} = \mathbf{E} + \delta\mathbf{E} \quad n_e = n_e + \delta n_e, \quad (8)$$

where $\delta\mathbf{E}$ and δn_e are the fluctuating components of the electric field and plasma density, respectively. Substituting these into Eq. 9 and averaging over the fluctuation period, we find

$$\frac{\partial}{\partial t}(m_e n_e \mathbf{u}_e) + \nabla \cdot (m_e n_e \mathbf{u}_e \otimes \mathbf{u}_e) = q n_e (\mathbf{E} + \mathbf{u}_e \times \mathbf{B}) - \nabla \cdot \mathbf{\Pi}_e - \nu_{e,c} m_e n_e \mathbf{u}_e + q \langle \delta n_e \delta \mathbf{E} \rangle \quad (9)$$

We see that an additional term, $q \langle \delta n_e \delta \mathbf{E} \rangle$, has appeared. This term, which we define as \mathbf{R}_{ei} , acts as an additional force on the electrons. We can cast this in terms of an effective collision frequency by defining $\mathbf{R}_{AN} = -m_e \nu_{AN} n_e \mathbf{u}_e$ to obtain an expression for the anomalous electron collision frequency ν_{AN} :

$$\nu_{AN} = \frac{|\mathbf{R}_{AN}|}{m_e n_e |\mathbf{u}_e|} \text{ s}^{-1}. \quad (10)$$

To go further, we must find a way to relate the fluctuation-averaged quantities to other fluid quantities. Experiments have shown that Hall thruster plasma fluctuations seem to follow a modified ion-acoustic dispersion relation with discrete frequency peaks near electron cyclotron resonances[15]. The wave propagates primarily in the azimuthal (θ) direction. Under these assumptions, it can be shown that [10, 16]

$$\nu_{AN} = c_1 \frac{\gamma W}{m_e n_e c_s v_{de}} \text{ s}^{-1}, \quad (11)$$

where c_1 is a unitless constant, γ is the growth rate of the wave, W is the energy density of the wave, $c_s = \sqrt{T_e/m_i}$ is the ion sound speed, $v_{de} = |\mathbf{E} \times \mathbf{B}|/|\mathbf{B}|^2$ is the azimuthal electron $E \times B$ drift speed, m_i is the ion mass, T_e is the electron temperature in J, and Z is the ion charge number.

To relate γ and W to the local plasma properties, we need to make some further assumptions. For this, we employ the conservation equation for wave energy[8]

$$\frac{DW}{Dt} = \frac{\partial W}{\partial t} + (\mathbf{v}_g \cdot \nabla)W = 2W(\gamma - \omega_{loss}). \quad (12)$$

In the above, \mathbf{v}_g is the group velocity of the wave and ω_{loss} is the rate at which the wave loses energy to the plasma via damping. We assume the wave propagates with the ions as they convect downstream, so $\mathbf{v}_g \approx \mathbf{u}_i$, where \mathbf{u}_i is velocity of singly-charged ions. Rearranging terms and making the further assumption that $\partial W/\partial t \approx 0$, we find that

$$2\gamma W = \mathbf{u}_i \cdot \nabla W + 2\omega_{loss} W. \quad (13)$$

We can now substitute the above expression into Eq. 11 and fold the factor of two into c_1 to get our closure model master equation

$$\nu_{AN} = c_1 \frac{\mathbf{u}_i \cdot \nabla W + 2\omega_{loss} W}{m_e n_e c_s v_{de}} \text{ s}^{-1}. \quad (14)$$

Armed with this expression, all that we need to obtain closure models for the anomalous collision frequency is to derive suitable expressions for the damping frequency ω_{loss} and wave energy density W .

A. Closure models

We consider five models in this paper, each of which has been derived from the Eq. 14. In contrast to some previous work, here we assume the wave energy saturates at the electron drift energy density, i.e. $W \propto m_e n_e v_{de}^2$ instead of the electron thermal energy. We then make several different assumptions for the scaling of ω_{loss} . In model A we assume that $\omega_{loss} = 0$, i.e. that there is no collisional or Landau damping and that convection is the sole loss mechanism. In models B and C, we assume that the wave can lose energy to ion Landau damping. The ion Landau damping rate for an ion acoustic-like wave with wavenumber k can be approximated as[17]

$$\omega_i = -k c_s \sqrt{\frac{\pi}{8}} \left[\sqrt{\frac{Z m_e}{m_i}} + \left(\frac{Z T_e}{T_i} \right)^{\frac{3}{2}} \exp \left(-\frac{Z T_e}{2 T_i} - \frac{3}{2} - 3 \frac{T_i}{Z T_e} \right) \right]. \quad (15)$$

In the above, we define T_i to be the temperature of singly-charged ions. For our analysis, we assume the majority of the growth occurs at a single wavenumber. In model B, we assume that frequency of maximum growth is the plasma frequency, so that $k \approx 1/\sqrt{2}\lambda_{de}$ [16]. This gives a damping rate of:

$$\omega_i = -\frac{\sqrt{\pi}\omega_{pe}}{4} \left[\frac{Zm_e}{m_i} + \sqrt{\frac{Zm_e}{m_i}} \left(\frac{ZT_e}{T_i} \right)^{\frac{3}{2}} \exp\left(-\frac{ZT_e}{2T_i} - \frac{3}{2} - 3\frac{T_i}{ZT_e}\right) \right] \quad (16)$$

For Xenon and Krypton, $m_e/m_i = 4.178 \times 10^{-6}$ and 6.546×10^{-6} , respectively so we neglect the first term in the brackets and arrive at our final expression for the ion Landau damping rate:

$$\omega_{loss} \propto \omega_{pe} \sqrt{\frac{Zm_e}{m_i}} \left(\frac{ZT_e}{T_i} \right)^{\frac{3}{2}} \exp\left(-\frac{ZT_e}{2T_i} - \frac{3}{2} - 3\frac{T_i}{ZT_e}\right) \quad (17)$$

In model C, we instead assume that the frequency of maximum growth is an electron cyclotron resonance. This gives a loss rate of

$$\omega_{loss} \propto \frac{\omega_{pe}}{M_e} \sqrt{\frac{Zm_e}{m_i}} \left(\frac{ZT_e}{T_i} \right)^{\frac{3}{2}} \exp\left(-\frac{ZT_e}{2T_i} - \frac{3}{2} - 3\frac{T_i}{ZT_e}\right), \quad (18)$$

where $M_e = v_{de}/c_e$ is the electron Mach number and $c_e = \sqrt{T_e/m_e}$ is the electron sound speed. In models D and E, we investigate the effects of classical collisions on the wave energy. In model D we assume that electron-ion collisions damp the wave, with a damping term of

$$\nu_{ei} = \frac{Z^2 e^4 n_i \ln \Lambda}{(4\pi\epsilon_0)^2 m_e^{1/2} T_e^{3/2}} \quad (19)$$

$$\omega_{loss} \propto \nu_{ei}, \quad (20)$$

where $\ln \Lambda$ is the Coulomb logarithm. For model E, we consider ion-neutral charge exchange (CEX) collisions instead of electron-ion collisions. For the purposes of computing the charge exchange collision frequency, both ions and neutrals are assumed to be cold, with the resulting damping rate having the form

$$\nu_{in,CEX} = n_n u_{in} \sigma_{CEX} \quad (21)$$

$$u_{in} = \frac{v_{th,i}}{\sqrt{\pi}} \left[\exp(-\tilde{u}_i^2) + \frac{\sqrt{\pi}}{2} \left(2\tilde{u}_i + \frac{1}{\tilde{u}_i} \right) \text{erf}(\tilde{u}_i) \right] \quad (22)$$

$$\tilde{u}_i = \frac{|\mathbf{u}_i|}{v_{th,i}} \quad (23)$$

$$\sigma_{CEX} = 10^{-20} \frac{1}{Z} \left[A - B \log\left(\frac{m_i}{q_e} u_{in}^2\right) \right] \quad (24)$$

$$\omega_{loss} \propto \nu_{in,CEX}. \quad (25)$$

In the above, n_n is the neutral density, u_{in} is the effective ion-neutral collision velocity, $v_{th,i}$ is the ion thermal speed, equal to $\sqrt{2T_i/m_i}$, \tilde{u}_i is the magnitude of the ion velocity normalized by the thermal speed, σ_{CEX} is charge exchange collision cross section as a function of kinetic energy, and A and B are numerical fit coefficients. For xenon, Miller et al.[18] found $A = 87.3$ and $B = 13.6$, while for krypton, Hause et al.[19] found $A = 80.7$ and $B = 14.7$.

With our closure models defined, we now describe the methods employed in our work, including the thruster being simulated, the experimental operating conditions, and details of the fluid code used for our simulations.

V. Methods

A. Thruster and experimental data

In this work, we compare our simulations to experimental measurements of the H9 Hall thruster. This is a magnetically-shielded 9-kW Hall thruster developed by the University of Michigan, the Jet Propulsion Laboratory, and the Air Force Research Laboratory.[20, 21]. In Fig. 2 we depict the thruster operating on Krypton in the University of

Model	Loss mechanisms	Expression for ν_{AN}
A	Convection	$\nu_{AN} = c_1 \frac{ \mathbf{u}_i \cdot \nabla(n_e v_{de}^2) }{n_e c_s v_{de}}$
B	Convection, Landau damping at ω_{pe}	$\nu_{AN} = c_1 \left[\frac{ \mathbf{u}_i \cdot \nabla(n_e v_{de}^2) }{n_e c_s v_{de}} + c_2 \omega_{pe} M_e \left(\frac{Z T_e}{T_i} \right)^{3/2} \exp \left(-\frac{1}{2} \frac{Z T_e}{T_i} - \frac{3}{2} - 3 \frac{T_i}{Z T_e} \right) \right]$
C	Convection, Landau damping at $\frac{\omega_{ce}}{M_e}$	$\nu_{AN} = c_1 \left[\frac{ \mathbf{u}_i \cdot \nabla(n_e v_{de}^2) }{n_e c_s v_{de}} + c_2 \omega_{ce} \left(\frac{Z T_e}{T_i} \right)^{3/2} \exp \left(-\frac{1}{2} \frac{Z T_e}{T_i} - \frac{3}{2} - 3 \frac{T_i}{Z T_e} \right) \right]$
D	Convection, $e - i$ collisions	$\nu_{AN} = c_1 \left[\frac{ \mathbf{u}_i \cdot \nabla(n_e v_{de}^2) }{n_e c_s v_{de}} + c_2 \sqrt{\frac{m_i}{m_e}} M_e v_{ei} \right]$
E	Convection, CEX collisions	$\nu_{AN} = c_1 \left[\frac{ \mathbf{u}_i \cdot \nabla(n_e v_{de}^2) }{n_e c_s v_{de}} + c_2 \sqrt{\frac{m_i}{m_e}} M_e v_{in,CEX} \right]$

Table 1 Summary of investigated models

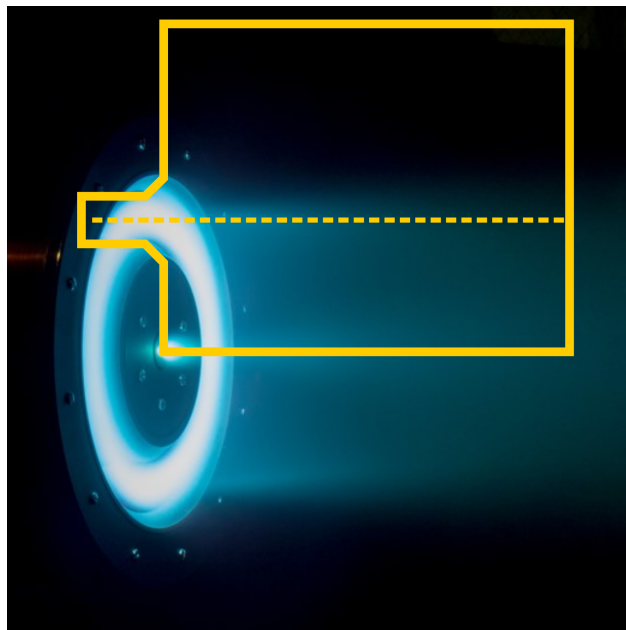


Fig. 2 H9 Hall thruster with overlaid simulation domain (solid line) and channel centerline (dashed line)

Parameter	Value
Maximum CFL number	0.9
# MFAM cells	2176
# Cartesian cells	1909
Anode mass flow rate	14.8 mg/s
Cathode flow fraction	7%
Cathode ionization fraction	5%
Anomalous collision frequency floor	$10^{-4}\omega_{ce} \text{ s}^{-1}$

Table 2 Simulation parameters employed in this work for the 300 V, 15 A case

Michigan’s Large Vacuum Test Facility (LVTF), with the domain of our simulations overlaid. We compare the results of our simulations to experimental measurements of the thrust, anode efficiency and ion velocity profile of the H9 operating at 300 V discharge voltage and 15 A discharge current on Xenon propellant. The ion velocity profile was obtained via non-invasive laser-induced fluorescence measurements.

B. Fluid code

All simulations in this work were performed using Hall2De, a two-dimensional axisymmetric ($z - r$) multi-fluid/hybrid-PIC Hall thruster code developed by the Jet Propulsion Laboratory and leveraged extensively for Hall thruster design and qualification[22–24]. In the version used in the present work, Hall2De solves both the ions and electrons as fluids. Ion and electron momentum in the azimuthal direction are also considered. Electron inertia is neglected, leading to a generalized Ohm’s law formulation for electron momentum. Energy equations for both ions and electrons are included. Neutrals are solved kinetically using a line-of-sight view factor algorithm.

As electron dynamics in Hall thrusters are highly anisotropic and intrinsically tied to the orientation of the guiding applied magnetic field lines, Hall2De solves the electron fluid equations on a magnetic field-aligned mesh (MFAM) in order to reduce the impact of numerical diffusion. While advantageous, this meshing strategy introduces other numerical challenges. Most critically, the field-aligned meshing strategy can lead to poor mesh quality near thruster boundaries and in regions of high magnetic field strength. This issue is most pronounced near the magnetic poles of the Hall thruster, where the magnetic field lines converge and cell sizes become necessarily very small. By the Courant-Friedrichs-Levy (CFL) condition, this in turn can severely restrict the ion timestep, increasing the time required to run the simulation. However, since the ions in Hall thrusters are approximately unmagnetized, they can instead be solved on a structured Cartesian mesh instead of on the MFAM. This enables more uniform cell sizes throughout the domain and significantly increases the maximum timestep of the simulation.

In the present work, we use a MFAM with 2176 cells and a Cartesian grid with 1909 cells. This resolution was selected after a grid convergence study. The timestep is set globally by the CFL condition,

$$\Delta t = \min_{i \in \text{cells}} \text{CFL}_{\text{max}} \frac{\lambda_{\text{max},i}}{\Delta x_i}, \quad (26)$$

where Δt is the timestep, CFL_{max} is a user-configurable maximum allowed CFL number, $\lambda_{\text{max},i}$ is the maximum ion wave speed in cell i , and Δx_i is a measure of size of cell i . In our case, we set Δx_i to the the ratio of cell volume to cell surface area. With the chosen mesh resolution and a maximum CFL number of 0.9, simulation time steps were on the order of 50 nanoseconds.

In addition to simulating multiple ion charge states, Hall2De can also simulate multiple ion fluids. In our case, we simulate two fluids—one corresponding to the ion beam and one to the ions emanating from the cathode. Ions created at different potential levels may also be assigned to different fluids, but we do not utilize this capability in this paper.

The remaining simulation parameters are summarized in Tab. 2.

C. Model calibration

All of the models described in Tab. 1 feature one or more numerical fit coefficients that must be calibrated in order to match data. For models with a single fit coefficient like model A, a fairly coarse parameter sweep of c_1 would suffice for this purpose, but for those with two fit coefficients, we would need to evaluate the models at a grid of test points

instead. This quadratically increases the number of simulations that need to be run. It would be preferable to only need to calibrate at most one (or ideally zero) coefficients per model.

To this end, we introduce in this paper a simple on-line calibration procedure for one of the anomalous transport coefficients (in this case, c_1). We employ a proportional-integral (PI) controller built into Hall2De to automatically adjust c_1 as the simulation progresses until the time-averaged discharge current matches experiment. To mitigate the effects of initial transients, we evaluate time-averaged quantities such as the discharge current using an exponential moving average as opposed to a simple average over all times. For the discharge current, this has the form:

$$I_{D,avg}(t_n) = \alpha_n I_D(t_n) + (1 - \alpha_n) I_{D,avg}(t_{n-1}) \quad (27)$$

$$\alpha_n = 1 - \exp\left(-\frac{\Delta t_n}{\tau}\right). \quad (28)$$

In the above, $I_{d,avg}(t_n)$, α_n , and Δt_n are the average discharge current, exponential smoothing coefficient, and timestep, respectively at iteration n and time t_n and τ is a user-adjustable time constant. The discrete form of the PI controller is given by

$$\log c_1(t_n) = \log c_1(t_{n-1}) + K_p \left[\left(1 + \frac{\Delta t_n}{T_i}\right) e(t_n) - e(t_{n-1}) \right]. \quad (29)$$

Here, K_p is the proportionality constant and T_i is the integral timescale. Following numerical experiments in a one-dimensional Hall thruster code, we set K_p to 0.06 and $T_i = \tau = 0.4$ ms. This choice of τ has the advantage of averaging the discharge current over multiple breathing mode cycles, so the controller does not try to damp out these oscillations. In Fig. 3, we show the results of one of our numerical experiments on a one-dimensional simulation of the H9 Hall thruster at 300 V and 15 A using a simple two-zone anomalous collision frequency model of the form:

$$v_{AN} = \begin{cases} c_1 \omega_{ce}/16 & z < L_{ch} \\ c_1 \omega_{ce}/160 & z \geq L_{ch}. \end{cases} \quad (30)$$

In Fig. 3a, we show the results of an initial simulation with $c_1 = 3$. The simulation reaches to a non-oscillatory steady state with an average discharge current of 30 A. In Fig. 3b, we show the results of applying our PI controller to c_1 . We let the simulation settle for 0.2 ms before turning on the controller. After 2 ms, the controller drives the simulation into a stable breathing mode oscillation with a mean current of 15 A and a peak to peak amplitude of 32 A. In Fig. 3c, we show how the value of c_1 changes over time in the controlled simulation. We see that c_1 declines rapidly until $t = 1$ ms, after which it stabilizes into an oscillation about its final mean value. In order to demonstrate that this small oscillation does not artificially drive the observed breathing mode oscillations, we perform a final simulation in which we fix the value of c_1 at 0.813, which was mean value that the controller found (red dashed line in Fig. 3c). We find that the uncontrolled simulation exhibited the same oscillations as the controlled simulation, albeit with a slightly larger peak to peak amplitude of 37 A.

This proof of concept has shown that the PI controller can successfully tune the magnitude of the anomalous collision frequency to match a target value, even in the case of quite strong breathing mode oscillations of $> 200\%$ peak to peak amplitude. The final value of c_1 may oscillate, but these oscillations have a negligible effect on the breathing mode oscillations exhibited by the plasma. Additionally, once c_1 converges to a stationary value, the PID controller can be turned off and the simulation continued with a static value of c_1 .

To calibrate c_2 , the damping rate scale coefficient, we perform a parameter sweep in the range of 0.1 – 100 with 11 simulations distributed logarithmically. For models which do not have a second coefficient, this step is not required.

This combination of online and offline calibration methods allows us to optimize our closure model fit coefficients efficiently and effectively using the smallest number of simulations possible. With this final step complete, we now turn to presenting our results for each of the ten closure models

D. Metrics for evaluating simulations

To compare our simulations to experiment, we consider four metrics. The first is the thrust, which is the net force on the thruster. We compute this by integrating the axially-directed momentum flux flowing out of the boundaries of the thruster.

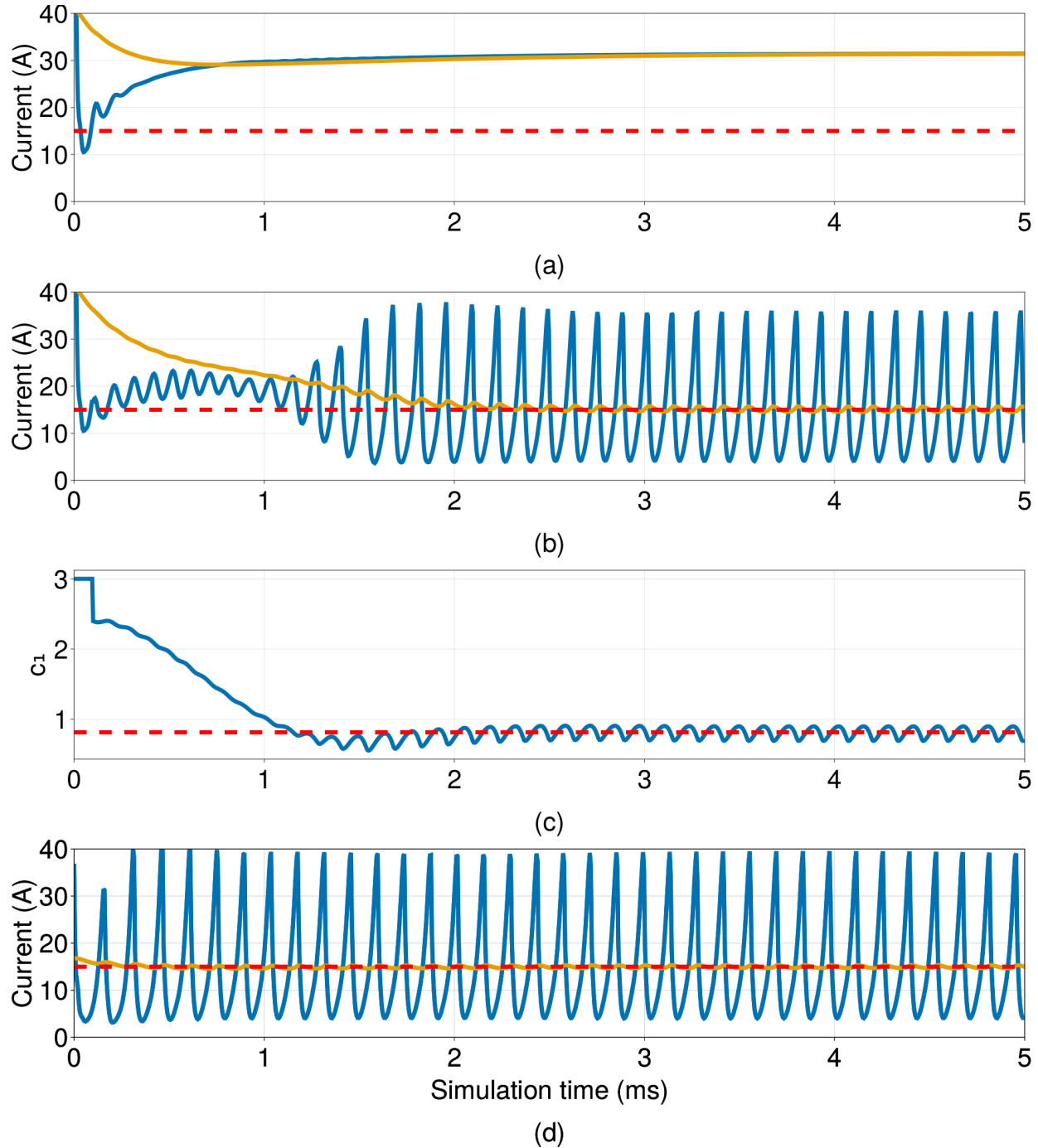


Fig. 3 Results of test of PI controller in 1D fluid Hall thruster code. (a) Discharge current (blue) and exponential moving average of discharge current (yellow) with $c_1 = 3$ and no control. (b) Discharge current with active PI control. Setpoint of 15 A shown as red dashed line. (c) Time history of c_1 for controlled simulation shown in (b). Final mean value of c_1 shown as red dashed line. (d) Discharge current with no control using mean c_1 found by controller in (c).

Model	Optimal c_1	Optimal c_2	Optimal η_a	Optimal IVE
A	0.490	N/A	59.4%	0.444
B	0.420	0.1	57.6%	0.443
C	0.470	0.1	59.3%	0.446
D	0.476	0.1	56.6%	0.446
E	0.451	0.25	59.3%	0.445

Table 3 Optimal coefficient values and performances for the models investigated in this work.

$$T = \iint_{\text{outflow}} \sum_{f=1}^2 \sum_{j=0}^3 m_i n_{f,j} u_{z,f,j} (\mathbf{u}_{f,j} \cdot d\mathbf{A}). \quad (31)$$

Here, $\mathbf{u}_{f,j}$ is the velocity of the species belonging with to fluid f and having charge j , $u_{z,j,f}$ and $n_{i,f,j}$ are the axial component of the velocity and the number density, respectively, of that species, and $d\mathbf{A}$ is the differential surface area vector. The second metric is the discharge current. As discussed in the previous section, this is actively controlled in order to match experiment. We compute the discharge current by integrating the net current density over the anode boundary surface, giving us

$$I_D = \iint_{\text{anode}} \left[\left(\sum_{f=1}^2 \sum_{j=1}^3 j q_e n_{f,j} \mathbf{u}_{f,j} \right) - \mathbf{j}_e \right] \cdot d\mathbf{A}, \quad (32)$$

where, $\mathbf{j}_e = q_e n_e \mathbf{u}_e$ is the electron current density vector (not including the azimuthal current). The third metric we consider is the anode efficiency, η_a , which measures how much the the discharge power is able to be converted into usable thrust power. It is computed as

$$\eta_a = \frac{T^2}{2\dot{m}_a I_D V_D}, \quad (33)$$

where \dot{m}_a is the mass flow rate of propellant through the anode and V_D is the discharge voltage. Since the discharge current of all simulations in this work is fixed at 15 A by our calibration procedure, we can use the anode efficiency as a direct proxy for thrust. Finally, to quantify how well our simulations match LIF measurements of the ion velocity, we employ the *integrated velocity error*, or IVE

$$\text{IVE} = \sqrt{\frac{\int_{z_0}^{z_N} (u_{1,1}(z) - u_{i,LIF}(z))^2 dz}{\int_{z_0}^{z_N} u_{i,LIF}^2(z) dz}}. \quad (34)$$

In this expression, z_0 and z_N are the first and last axial locations where LIF data is available, $u_{1,1}$ is the simulated axial velocity of singly-charged ions from the first fluid, i.e. the main beam, and $u_{i,LIF}$ is the LIF measurement of the same. This metric is defined such that a higher integrated velocity error means that the simulation agrees less well with data. For example, an IVE of 0.3 suggests that the simulated ion velocity profile is, on average, 30% different from the measured profile. With these metrics defined, we now turn to presenting the results of our study.

VI. Results and Discussion

In Fig. 4, we present the results of our study. We were unable to obtain converged solutions for model C with $c_2 > 50$ and model D with $c_2 > 10$. All simulations had a discharge current within 0.5 A of the target value of 15 A. We compare the simulated anode efficiencies (Fig. 4a) and integrated velocity errors as a function of the second fit coefficient c_2 to experimental values, as well as to a calibrated reference simulation of the H9 at 300 V and 15A.

First examining the anode efficiencies, all models were able to match the experimental anode efficiency of 64% to within 10% at low values of c_2 . The best-performing model was model A (convection with no damping term) with an anode efficiency of 59.4%. In the limit of low c_1 , the other models approached result of model A, but none were able to improve upon it. As c_2 increased and thus the damping term became dominant over the convection term in models B - E, the efficiency monotonically decreased. The worst obtained efficiency was 24%, seen in model C (convection with ion

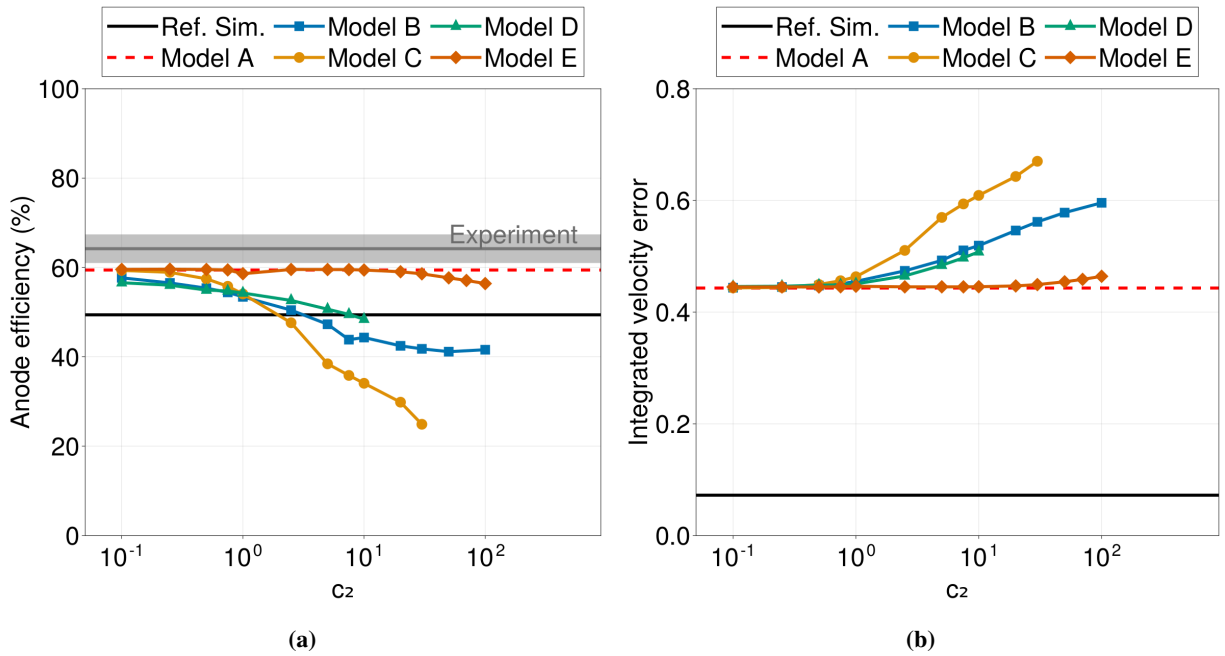


Fig. 4 (a) Anode efficiency and (b) integrated velocity error as a function of fit coefficient c_2 for all models. Experimental anode efficiency is indicated as a grey shaded region in (a).

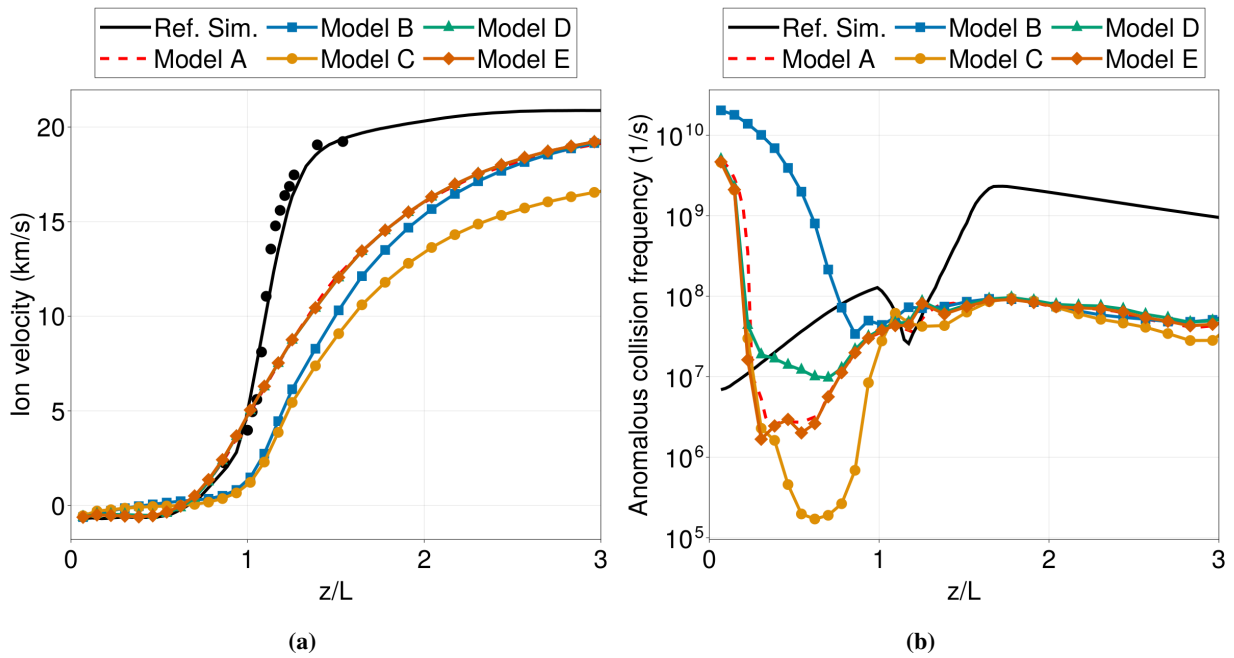


Fig. 5 (a) Ion velocity and (b) anomalous collision frequency along channel centerline for best-performing cases of each model. LIF data is represented as discrete black circular markers in (a).

Landau damping at cyclotron resonances) at high values of c_2 . Interestingly, all models were able to improve upon the anode efficiency of the reference simulation at low values of c_2 . Calibrated stationary anomalous collision frequency profiles such as the one employed for the reference simulation often have difficulty matching experimental thrust values [23, 25], so this is an encouraging result. However, these empirically-inferred profiles are typically calibrated to match the discharge current and ion velocity profile, not the thrust, so it is possible that further calibration could rectify this discrepancy.

Next, we examine the integrated velocity errors. For all models except for model G, this was constant at roughly 0.45 for $0 < c_2 < 1.0$. For $c_2 > 1.0$, the IVE increased for all models in ways that mirrored the trends in efficiency. To better understand why the integrated velocity errors are so similar across all of the models, we plot in Fig. 5 the axial component of the ion velocity (Fig. 5a) and the anomalous collision frequency (Fig. 5b) extracted along the discharge channel centerline for the cases with the highest anode efficiency for each model. These best-fit coefficients are summarized in Tab. 3. As expected from the IVEs, the ion velocity profiles for all models are very similar. Models A, D, and E are indistinguishable from each other, while models B and C are somewhat different, with acceleration happening a tenth of a thruster length later than the other simulations. In all cases, the ion acceleration is more relaxed than that of the experimental data and reference simulation.

To understand the structure of the ion acceleration profiles, we now turn to examining the time-averaged anomalous collision frequency along the channel centerline. In all cases, the anomalous collision frequency starts high, then declines to a minimum before recovering somewhat. This qualitatively matches the shape of the empirically-inferred anomalous collision frequency profile used to generate the reference simulation. However, the collision frequency is generally at least an order of magnitude lower than the empirical profile, with the exception of near the anode, where it is two to three orders of magnitude higher. Downstream of the thruster exit plane ($z/L = 1$), all five models attain a nearly constant collision frequency of 10^8 s^{-1} . However, the models differ from each other by several orders of magnitude upstream of this location. Models A and E are indistinguishable from one another, with a minimum occurring at $z/L \approx 0.5$. For model D, the trough in collision frequency is shallower than in models A and E by an order of magnitude. For model B, the collision frequency is much higher upstream than the other models, with a shallow minimum around $z/L = 0.9$. As the location of the minimum in collision frequency coincides with the location of the peak electric field strength in Hall thrusters, this feature explains the delayed acceleration profile seen in model B. For model C, the minimum collision frequency is an order of magnitude deeper than models A and E. The location of the minimum in most models is near $z/L = 0.5$, which is nearly coincident with the ion stagnation point, where $u_i = 0$, where the convection term should be minimized. Taken with the efficiency and integrated velocity error data, these results reinforce the idea that the convection term dominates the damping terms, especially downstream of the exit plane.

The high value of the collision frequency near the anode was also observed by Lafleur et al [10] in their analytical model, which shares a similar derivation to ours. It likely stems from the fact that the ion sound speed c_s and electron drift velocity v_{de} are both low near the anode, causing the value of the collision frequency to grow rapidly in this region. To fix this, they cut off the anomalous collision frequency near the anode, with the justification that the wave may not be saturated before the ion stagnation point. With this modification, the magnitude of the collision frequency downstream of the anode minimum would likely need to increase by an order of magnitude in order to match the target discharge current. However, it is not assured that our simulations need to match the empirical reference profile in order to give good results, as these profiles are known in general to be non-unique [26] and may not correspond well with the actual value of the anomalous collision frequency in Hall thrusters. Nevertheless, a different model may be necessary in the near anode region in order to account for differences in the level of wave saturation.

The other major difference between our model predictions and the empirical reference profile is the location of the minimum collision frequency. To better match experiment, it would need to be shifted half a thruster length downstream from its present location. One possible way to achieve this would be if the group velocity of the wave in the axial direction was not $u_{i,z}$ but $u_{i,z} - c_s$. This might shift the minimum to the ion sonic point instead of the ion stagnation point. In the experimental data, the ion sonic point sits just inside of the channel, near $z/L = 0.9$, while in our simulations, it sits between $z/L = 0.75$ and $z/L = 1.1$. This is still likely too far upstream, but would be an improvement over the present results. More technically, the group velocity of a wave is given by:

$$\mathbf{v}_g = \frac{\partial \omega}{\partial \mathbf{k}}, \quad (35)$$

where ω is the real frequency of the wave and \mathbf{k} is the wave-vector of propagation. For an ion acoustic instability with

drifting ions with a velocity vector \mathbf{u}_i , the real frequency is given by[8, 10]

$$\omega = \mathbf{k} \cdot \mathbf{u}_i \pm \frac{k c_s}{\sqrt{1 + k^2 \lambda_{de}^2}}. \quad (36)$$

In our previous analysis and in experiments, k is primarily in the azimuthal direction, so the sound speed contribution should be very small in the axial direction. However, here we make the assumption that the wave propagates in the same direction as the ions and thus the group velocity for a wave with wavenumber k is[10]

$$\mathbf{v}_g = \mathbf{u}_i \pm \frac{c_s}{(1 + k^2 \lambda_{de}^2)^{3/2}} \hat{u}_i, \quad (37)$$

where $\hat{u}_i \equiv \mathbf{u}_i / |\mathbf{u}_i|$ is the unit vector of ion propagation. If the majority of the growth occurs at a single wavenumber and the wavenumber of maximum growth that given by the ion acoustic dispersion relation (i.e. $k^2 \lambda_{de}^2 = \frac{1}{2}$), then we arrive at

$$\mathbf{v}_g = \mathbf{u}_i \pm \sqrt{\frac{8}{27}} c_s \hat{u}_i \approx \mathbf{u}_i \pm 0.544 c_s \hat{u}_i. \quad (38)$$

We can thus see that there may be some theoretical justification for shifting the profile forward by a factor of c_s . We also note that when implementing the model of Lafleur, Baalrud and Chabert[10], we found that the minimum of the collision frequency occurred significantly further downstream than in the empirical reference simulation. That model was similar to ours in all respects except for the assumption that the wave saturated at some fraction of the plasma thermal energy density rather than the electron drift kinetic energy density. Combined with a more complete expression for the group velocity and improved modeling near the anode, it may be that allowing the wave to saturate at a fraction of the electron *total* energy density ($W \propto 3 n_e T_e + m_e n_e v_{de}^2$) might cause the minimum in the anomalous collision frequency to move to a location intermediate between that predicted by the drift and thermal energy assumptions alone. However, the thermal energy typically dominates the drift kinetic energy, so it is possible that the result would be similar to that predicted by Lafleur et al.

Overall, while we were unable to quantitatively match ion velocity measurements, we were able to obtain good agreement with the experimental anode efficiency values and qualitative agreement with some key features of the empirically-inferred anomalous collision frequency profile. The models investigated in this work have performed the best out of those that we have yet evaluated[12, 13, 27]. While still not completely predictive, these models suggest that it may not be impossible to self-consistently account for anomalous transport in Hall thrusters in a fluid framework.

VII. Conclusion

In this work, we evaluated five algebraic closure models of the Hall thruster anomalous transport. We assumed that the instability responsible for this transport saturated at the electron drift kinetic energy, and that the primary loss mechanism was convection of the wave energy out of the thruster. We investigated the effect of several additional damping mechanisms, including classical electron-ion and ion-neutral charge exchange collisions, in addition to ion Landau damping at both the plasma frequency and at cyclotron resonances. We found that these secondary damping mechanisms were insignificant compared to convection, and that as a result all of these models produced similar estimates of the thruster anode efficiency and the error in the ion velocity compare to experiment.

Despite significant differences in the ion velocity profiles between our simulations and experimental measurements obtained via laser-induced fluorescence measurements of the H9 Hall thruster, the anode efficiencies predicted by our simulations were very close to the experimental values, something which previous closure models have not yet been able to attain. In addition, the predicted anomalous collision frequency profiles shared many features in common with empirically-inferred collision frequency profiles for this thruster. While these results have not yet been extended to other thrusters or operating conditions, they suggest that algebraic closure models of the anomalous collision frequency may be able to capture major features of the Hall thruster discharge plasma in a predictive manner.

Acknowledgments

We would like to thank Dr. Ioannis Mikellides and Dr. Alejandro Lopez Ortega of the Jet Propulsion Laboratory for allowing us to use Hall2De. We would additionally like to thank Ms. Leanne Su for calibrating the reference simulation

of the H9 used in this work. The majority of the simulations used in this work were carried out on the Great Lakes computing cluster, managed by Advanced Research Computing, a division of the University of Michigan's Information and Technology Services. This work was in part supported by the AFOSR Space Propulsion and Power portfolio, FA9550-19-1-0022.

References

- [1] Hofer, R. R., Lobbia, R., Chaplin, V., Ortega, A. L., Mikellides, I., Polk, J., Kamhawi, H., Frieman, J., Huang, W., Peterson, P., and Herman, D., "Completing the Development of the 12.5 kW Hall Effect Rocket with Magnetic Shielding (HERMeS)," *36th International Electric Propulsion Conference*, 2019, pp. IEPC-2019-193.
- [2] Jackson, J., Allen, M., Myers, R., Soendker, E., Welander, B., Tolentino, A., Hablitzel, S., Yeatts, C., Sheehan, C., Cardin, J., Snyder, J. S., Hofer, R. R., Tofil, T., and Herman, D., "13kW Advanced Electric Propulsion Flight System Development and Qualification," *The 36th International Electric Propulsion Conference*, 2019, p. 18. URL https://iepc2017.org/sites/default/files/speaker-papers/iepc-2017-223_aeps_development_and_qualification.pdf.
- [3] Frieman, J. D., Kamhawi, H., Huang, W., Mackey, J., Ahern, D. M., Peterson, P. Y., Gilland, J., Hall, S. J., Hofer, R. R., Inaba, D., Dao, H., Zubair, J., Neuhoff, J., and Branch, N. A., "Characterization test of the 12.5-kw advanced electric propulsion system engineering test unit hall thruster," 2020. <https://doi.org/10.2514/6.2020-3626>.
- [4] Snyder, J. S., Goebel, D. M., Chaplin, V., Ortega, A. L., Mikellides, I. G., Aghazadeh, F., Johnson, I., Kerl, T., and Lenguito, G., "Electric Propulsion for the Psyche Mission," *36th International Electric Propulsion Conference*, 2019.
- [5] Snyder, J. S., Chaplin, V., Goebel, D. M., Hofer, R. R., Ortega, A. L., Mikellides, I. G., Kerl, T., Lenguito, G., Aghazadeh, F., and Johnson, I., "Electric propulsion for the psyche mission: Development activities and status," *AIAA Propulsion and Energy 2020 Forum*, 2020, pp. 1-15. <https://doi.org/10.2514/6.2020-3607>, URL <https://arc.aiaa.org/doi/10.2514/6.2020-3607>.
- [6] Walker, J. A., Frieman, J. D., Walker, M. L., Khayms, V., King, D., and Peterson, P. Y., "Electrical facility effects on hall-effect-thruster cathode coupling: Discharge oscillations and facility coupling," *Journal of Propulsion and Power*, Vol. 32, 2016, pp. 844-855. <https://doi.org/10.2514/1.B35835/ASSET/IMAGES/LARGE/FIGURE14.JPEG>, URL <https://arc.aiaa.org/doi/10.2514/1.B35835>.
- [7] Frieman, J. D., Liu, T. M., and Walker, M. L., "Background flow model of hall thruster neutral ingestion," *Journal of Propulsion and Power*, Vol. 33, 2017, pp. 1087-1101. <https://doi.org/10.2514/1.B36269/ASSET/IMAGES/LARGE/FIGURE14.JPEG>, URL <https://arc.aiaa.org/doi/10.2514/1.B36269>.
- [8] Davidson, R. C., and Krall, N. A., "Anomalous transport in high-temperature plasmas with applications to solenoidal fusion systems," *Nuclear Fusion*, Vol. 17, 1977, p. 6.
- [9] Cappelli, M. A., Young, C. V., Cha, E., and Fernandez, E., "A zero-equation turbulence model for two-dimensional hybrid Hall thruster simulations," *Physics of Plasmas*, Vol. 22, 2015. <https://doi.org/10.1063/1.4935891>.
- [10] Lafleur, T., Baalrud, S. D., and Chabert, P., "Theory for the anomalous electron transport in Hall effect thrusters. I. Insights from particle-in-cell simulations," *Physics of Plasmas*, Vol. 23, 2016. <https://doi.org/10.1063/1.4948495>.
- [11] Ortega, A. L., Katz, I., and Chaplin, V. H., "Application of a first-principles anomalous transport model for electrons to multiple Hall thrusters and operating conditions," 2018. <https://doi.org/10.2514/6.2018-4903>, URL <http://arc.aiaa.org>.
- [12] Jorns, B., "Predictive, data-driven model for the anomalous electron collision frequency in a Hall effect thruster," *Plasma Sources Science and Technology*, Vol. 27, 2018. <https://doi.org/10.1088/1361-6595/aae472>.
- [13] Jorns, B. A., "Two Equation Closure Model for Plasma Turbulence in a Hall Effect Thruster," *36th International Electric Propulsion Conference*, 2019, pp. 1-12.
- [14] Kwon, K., "Analytical modeling of the anomalous electron collision frequency in partially magnetized $e \times B$ plasmas," *AIP Advances*, Vol. 11, 2021. <https://doi.org/10.1063/5.0059689>.
- [15] Cavalier, J., Lemoine, N., Bonhomme, G., Tsikata, S., Honoré, C., and Grésillon, D., "Hall thruster plasma fluctuations identified as the $E \times B$ electron drift instability: Modeling and fitting on experimental data," *Physics of Plasmas*, Vol. 20, 2013, p. 082107. <https://doi.org/10.1063/1.4817743>, URL <https://aip.scitation.org/doi/abs/10.1063/1.4817743>.
- [16] Davidson, R. C., and Krall, N. A., "Anomalous transport in high-temperature plasmas with applications to solenoidal fusion systems," *Nuclear Fusion*, Vol. 17, 1977, pp. 1313-1372. <https://doi.org/10.1088/0029-5515/17/6/017>.

- [17] McKinstrie, C. J., Giacone, R. E., and Startsev, E. A., "Accurate formulas for the Landau damping rates of electrostatic waves," *Physics of Plasmas*, Vol. 6, 1999, p. 463. <https://doi.org/10.1063/1.873212>, URL <https://aip.scitation.org/doi/abs/10.1063/1.873212>.
- [18] Miller, J. S., Pullins, S. H., Levandier, D. J., Chiu, Y. H., and Dressler, R. A., "Xenon charge exchange cross sections for electrostatic thruster models," *Journal of Applied Physics*, Vol. 91, 2002, pp. 984–991. <https://doi.org/10.1063/1.1426246>.
- [19] Hause, M. L., Prince, B. D., and Bemish, R. J., "Krypton charge exchange cross sections for Hall effect thruster models," *Journal of Applied Physics*, Vol. 113, 2013. <https://doi.org/10.1063/1.4802432>.
- [20] Hofer, R. R., Cusson, S. E., Lobbia, R. B., and Gallimore, A. D., "The H9 Magnetically Shielded Hall Thruster," 2017.
- [21] Cusson, S. E., Hofer, R. R., Lobbia, R. B., Jorns, B. A., and Gallimore, A. D., "Performance of the H9 Magnetically Shielded Hall Thrusters," 2017.
- [22] Mikellides, I. G., and Katz, I., "Numerical simulations of Hall-effect plasma accelerators on a magnetic-field-aligned mesh," *Physical Review E*, Vol. 86, 2012. <https://doi.org/10.1103/PhysRevE.86.046703>.
- [23] Ortega, A. L., and Mikellides, I. G., "The importance of the cathode plume and its interactions with the ion beam in numerical simulations of Hall thrusters," *Physics of Plasmas*, Vol. 23, 2016, p. 1411. <https://doi.org/10.1063/1.4947554>, URL <https://doi.org/10.1063/1.4947554>.
- [24] Ortega, A. L., Mikellides, I. G., Sekerak, M. J., and Jorns, B. A., "Plasma simulations in 2-D (r-z) geometry for the assessment of pole erosion in a magnetically shielded Hall thruster," *Journal of Applied Physics*, Vol. 125, 2019, p. 033302. <https://doi.org/10.1063/1.5077097>, URL <https://aip.scitation.org/doi/abs/10.1063/1.5077097>.
- [25] Su, L. L., Marks, T. A., and Jorns, "Investigation into the efficiency gap between krypton and xenon operation on a magnetically shielded Hall thruster." *International Electric Propulsion Conference*, 2022.
- [26] Mikellides, I. G., and Ortega, A. L., "Challenges in the development and verification of first-principles models in Hall-effect thruster simulations that are based on anomalous resistivity and generalized Ohm's law," *Plasma Sources Science and Technology*, Vol. 28, 2019, p. 48. <https://doi.org/10.1088/1361-6595/aae63b>, URL <https://doi.org/10.1088/1361-6595/aae63b>.
- [27] Marks, T. A., Ortega, A. L., Mikellides, I. G., and Jorns, B., "Self-consistent implementation of a zero-equation transport model into a predictive model for a Hall effect thruster," , ??? <https://doi.org/10.2514/6.2021-3424>, URL <https://arc.aiaa.org/doi/abs/10.2514/6.2021-3424>.